# Retrieving the Clear-Sky Vertical Longwave Radiative Budget from TOVS: Comparison of a Neural Network–Based Retrieval and a Method UsingGeophysical Parameters

F. Chevallier, F. Chéruy, Raymond Armante, C. Stubenrauch, N. Scott

▶ **To cite this version:**

F. Chevallier, F. Chéruy, Raymond Armante, C. Stubenrauch, N. Scott. Retrieving the Clear-Sky Vertical Longwave Radiative Budget from TOVS: Comparison of a Neural Network–Based Retrieval and a Method UsingGeophysical Parameters. Journal of Applied Meteorology, 2000, 39 (9), pp.1527-1543. ⟨10.1175/1520-0450(2000)0392.0.CO;2⟩. ⟨hal-02957650⟩

**HAL Id: hal-02957650**

**https://hal.science/hal-02957650v1**

Submitted on 24 Jan 2021

**HAL** is a multi-disciplinary open access archive for the deposit and dissemination of scientific research documents, whether they are published or not. The documents may come from teaching and research institutions in France or abroad, or from public or private research centers.

L'archive ouverte pluridisciplinaire **HAL**, est destinée au dépôt et à la diffusion de documents scientifiques de niveau recherche, publiés ou non, émanant des établissements d'enseignement et de recherche français ou étrangers, des laboratoires publics ou privés.

HAL Authorization

# Retrieving the Clear-Sky Vertical Longwave Radiative Budget from TOVS: Comparison of a Neural Network–Based Retrieval and a Method Using Geophysical Parameters

F. CHEVALLIER,* F. CHÉRUY,+ R. ARMANTE, C. J. STUBENRAUCH, AND N. A. SCOTT

*Laboratoire de Météorologie Dynamique du CNRS, École Polytechnique, Palaiseau, France*

(Manuscript received 17 February 1999, in final form 24 November 1999)

ABSTRACT

At a time when a new generation of satellite vertical sounders is going to be launched (including the Infrared Atmospheric Sounder Interferometer and Advanced Infrared Radiometric Sounder instruments), this paper assesses the possibilities of retrieving the vertical profiles of longwave clear-sky fluxes and cooling rates from the Television and Infrared Observation Satellite (TIROS) Operational Vertical Sounder (TOVS) radiometers aboard the polar-orbiting National Oceanic and Atmospheric Administration satellites since 1979. It focuses on two different methodologies that have been developed at Laboratoire de Météorologie Dynamique (France). The first one uses a neural network approach for the parameterization of the links between the TOVS radiances and the longwave fluxes. The second one combines the geophysical variables retrieved by the Improved Initialization Inversion method and a forward radiative transfer model used in atmospheric general circulation models. The accuracy of these two methods is evaluated using both theoretical studies and comparisons with global observations.

## 1. Introduction

The earth's atmosphere is being observed continuously by a network of various instruments. The satellite radiometers are among the most important of these instruments, because their mesh in both space and time is by far the most fine. Since 1979, the National Oceanic and Atmospheric Administration (NOAA) has been bringing an ambitious program of polar sun-synchronous satellites into operation: measurements have been made by various onboard instruments every 12 h for most parts of the world and at most times. In particular, the Television and Infrared Observation Satellite—Next Generation (TIROS-N) Operational Vertical Sounder (TOVS) package combines a wide range of infrared and microwave sounding channels spread on three radiometers: High-Resolution Infrared Radiation Sounder, second generation—20 channels (HIRS-2); Microwave Sounding Unit (MSU)—four channels; and Stratospheric Sounding Unit—three channels. TOVS can provide estimates of many geophysical variables: the three-dimensional temperature and moisture description of the atmosphere, a description of the surface (surface temperature and sea-ice detection), and various cloud properties (cloud type, cloud-top altitude, and effective cloudiness) (e.g., Smith et al. 1979; Susskind et al. 1997; Scott et al. 1999). The TOVS specifications also allow estimations of the longwave (LW) and shortwave boundary fluxes (e.g., Ellingson et al. 1989; Gupta 1989; Rossow and Zhang 1995; Mehta and Susskind 1999) and the three-dimensional LW structure of the atmosphere (Ellingson et al. 1994). Two main purposes motivate the production of these various datafields (the sounder brightness temperatures and the estimated geophysical and radiative parameters). The assimilation in numerical weather prediction schemes is the first one (e.g., Andersson et al. 1991). The second one is the analysis of climate, made possible by the continuity of the TOVS observations since 1979 (e.g., Wu et al. 1993; Wittmeyer and Vonder Haar 1994; Soden and Bretherton 1996; Stubenrauch et al. 1999c).

The current study focuses on two methodologies that have been developed at the Laboratoire de Météorologie Dynamique (LMD) for the estimation of the vertical LW radiative budget from TOVS. The first method relies on a nonlinear statistical method, the multilayer perceptron (MLP; Rumelhart et al. 1986), for directly linking the TOVS observed brightness temperatures to the LW fluxes: it will be referred to as N-TbFlux. The second meth-

* Current affiliation: European Centre for Medium-Range Weather Forecasts, Reading, Berkshire, United Kingdom.
+ Current affiliation: Laboratoire de Météorologie Dynamique, Paris, France.

*Corresponding author address:* F. Chevallier, ECMWF, Shinfield Park, Reading, Berkshire RG29AX, United Kingdom.
E-mail: chevallier@ecmwf.int

© 2000 American Meteorological Society

od combines the geophysical variables retrieved by the Improved Initialization Inversion (3I) method (Chédin et al. 1985) and a classical forward radiative transfer model (Morcrette 1991; Zhong and Haigh 1995): it will be referred to as 3IFlux. This article is restricted to the estimation of the clear-sky contribution to the LW radiative fluxes and cooling rates. Attention has been drawn to these quantities 1) because of their role in the atmospheric general circulation (e.g., Pierrehumbert 1995) and 2) in the current context of intensive research about water vapor feedbacks (e.g., Sinha and Harries 1997; Allan et al. 1999). These radiative quantities are described in section 2. A global continuous dataset such as the TOVS observations makes it possible to study their spatial and temporal variability. Because all existing databanks suffer from retrieval uncertainties, estimating the accuracy of schemes like the two discussed here is a delicate task. As a consequence, the validation of N-TbFlux and 3IFlux has been based mainly on synthetic cases and sensitivity studies. The results of these experiments are presented in sections 3 and 4, respectively, together with the description of each method. A final assessment of the uncertainty in the computed fluxes was made by comparisons of the flux and cooling rate estimations with space–time-coincident flux determinations: both direct computations from radiosonde data and Earth Radiation Budget Experiment (ERBE) products (Barkstrom 1984). These validations are presented respectively in sections 5 and 6. Section 7 summarizes the results and discusses the advantages and weaknesses of the two approaches.

## 2. Definitions

The formal solution of the radiative transfer equation for a stratified nonscattering atmosphere in local thermodynamic equilibrium is

$$F^{\uparrow}(P) = \pi \int_{-1}^{+1} \mu \, d\mu \int_{\nu} d\nu \left[ I_{\nu}^{\uparrow}(P_0, \mu)\tau_{\nu}(P_0, P, \mu) + \int_{P_0}^{P} B_{\nu}(T_{P'}) \frac{\partial \tau_{\nu}(P', P, \mu)}{\partial P'} \, dP' \right] \quad \text{and} \tag{1}$$

$$F^{\downarrow}(P) = \pi \int_{-1}^{+1} \mu \, d\mu \int_{\nu} d\nu \int_{0}^{P} B_{\nu}(T_{P'}) \frac{\partial \tau_{\nu}(P', P, \mu)}{\partial P'} \, dP'. \tag{2}$$

Here, $F^{\uparrow}(P)$ [$F^{\downarrow}(P)$] is the upward (downward) radiative flux at the pressure level $P$, integrated over the LW spectrum. The quantity $I_{\nu}^{\uparrow}(P, \mu)$ is the monochromatic radiance at frequency $\nu$ at pressure level $P$ propagating in a direction such that $\mu$ is the cosine of the zenith angle. Also, $P_0$ is the pressure at the surface, $B_{\nu}(T_P)$ is the Planck function at temperature $T_P$ at pressure level $P$, and $\tau_{\nu}(P', P, \mu)$ is the monochromatic flux transmittance for isotropic radiation between the pressure levels $P$ and $P'$.

The $F^{\uparrow}$s and the $F^{\downarrow}$s are the usual quantities computed by radiative transfer models. For climate studies, the net fluxes defined by $F(P) = F^{\uparrow}(P) - F^{\downarrow}(P)$ are more relevant parameters than $F^{\uparrow}$s and $F^{\downarrow}$s, when considered separately. Indeed, at each pressure level $P$, $F(P)$ is part of the energy budget. In particular, the LW surface net flux (LSNF) is added to other surface fluxes in the expression of the first derivative of the surface temperature as a function of time (e.g., Holton 1991). The net flux at the top of the atmosphere (TOA), usually referred to as outgoing longwave radiation (OLR), is also of special interest, because it represents the only loss of energy from the earth–atmosphere system. The difference between OLR and LSNF is the total LW cooling (TLC) of the atmosphere.

In the vertical, the temperature temporal variations are linked linearly to the net radiative flux divergence (in addition to the other diabatic terms and to the adiabatic cooling terms): the LW cooling rates $C_{\mathrm{LW}}(P)$, in K day$^{-1}$,

$$C_{\mathrm{LW}}(P) = -\frac{g}{C_p}\frac{\partial F(P)}{\partial P} = \frac{g}{C_p}\frac{\partial F^{\downarrow}(P)}{\partial P} - \frac{g}{C_p}\frac{\partial F^{\uparrow}(P)}{\partial P}, \tag{3}$$

where $C_p$ is the heat capacity at constant pressure, and $g$ is the gravitational acceleration.

The two codes to which reference is made in the current study, N-TbFlux and 3IFlux, compute the $F^{\uparrow}$s and the $F^{\downarrow}$s. The results shown here, however, focus on the estimation of the three radiative fluxes (OLR, LSNF, and TLC) and of the vertical cooling rates $C_{\mathrm{LW}}$. As said in the introduction, restriction is made to the clear-sky contribution to these quantities. With this approach, the computed LW fluxes follow Eqs. (1) and (2). The clear-sky LW cooling rates are calculated from the clear-sky fluxes with Eq. (3). This approach allows one to separate the contribution to the fluxes from atmospheric gases from that of the solid and liquid water, provided one knows the profiles of the gases in the cloudy regions.

## 3. Neural network–based flux retrieval from HIRS radiances

### *a. A neural network–based technique*

Many statistical methods have been developed in the past to infer links from a certain property of a real

+3,650/351-,5/.8(4734,./. !"#"! $%##&)+*

system (response or output) to another property of that system (predictor or input). These algorithms construct prediction rules by processing data taken from cases for which the values of both the response and the predictors have been determined. The most widespread technique is linear regression. For a long time, it has been applied to the estimation of fluxes and cooling rates from satellite data (e.g., Raschke et al. 1973; Gruber and Winston 1978; Tarpley 1979; Ellingson et al. 1994). The linear hypothesis on which these techniques are based limits the accuracy of such models.

Other statistical methods do not have the same drawback: for instance, MLP as defined by Rumelhart et al. (1986). MLP is among the artificial neural network techniques. It relies on processors, called formal neurons or neurons, with reference to the biological analogy. A neuron computes a weighted sum of its inputs and transfers this signal through a sigmoidal function (here the hyperbolic tangent). The neurons are gathered in layers. One or more ''hidden'' layers of neurons may be introduced between the input layer and the output layer. The parameters of this system are determined in an iterative way during a learning phase, by using a nonlinear regression: the so-called back-propagation algorithm. Since the beginning of the 1990s, MLP increasingly has been used at LMD for meteorology-related problems (e.g., Escobar-Munoz et al. 1993; Rieu et al. 1996; Chevallier et al. 1998). In particular, a preliminary study showed encouraging results in estimating the clear-sky flux profiles from TOVS brightness temperatures at nadir and over oceans (Chéruy et al. 1996a). Based on this approach, the complete N-TbFlux scheme has been elaborated.

### b. Data preprocessing

N-TbFlux can estimate the radiative LW downward and upward flux profiles from TOA to the surface and from clear or cloud-cleared HIRS radiances. The cloud detection and cloud clearing of HIRS radiances are part of the 3I inversion. A summary of the 3I cloud detection, which is performed at HIRS spatial resolution (17 km at nadir), is given in Table 1 of Stubenrauch et al. (1999a). To reduce time-consuming computations, the HIRS radiances then are averaged separately over clear pixels and over cloudy pixels within 100-km by 100-km regions. If all pixels within such a region are cloudy, ''cloud-cleared'' radiances are inferred from the warmest pixels (Wahiche 1984; Chédin et al. 1985). The associated clear-sky LW flux profiles then can be computed from the clear or cloud-cleared HIRS radiances by the N-TbFlux method. At present, the 3I algorithm does not yet decontaminate the HIRS 4.57-$\mu$m channel from clouds, which is necessary for flux retrieval by N-TbFlux (see section 3d). In the near future, 3I will be extended for that purpose. Therefore, in the following article only real clear-sky situations are treated by N-TbFlux.

TABLE 1. The 20 pressure levels used for the radiative computations. They correspond to the pressure levels from the ECMWF operational general circulation model before 1991, when the surface pressure is equal to 1013 hPa.

| Level | Pressure (hPa) | Level | Pressure (hPa) |
|---|---|---|---|
| 19 | 0.0 | 9 | 453.1 |
| 18 | 20.0 | 8 | 546.7 |
| 17 | 40.0 | 7 | 642.4 |
| 16 | 60.8 | 6 | 735.3 |
| 15 | 86.2 | 5 | 820.4 |
| 14 | 119.7 | 4 | 892.8 |
| 13 | 163.6 | 3 | 948.5 |
| 12 | 219.2 | 2 | 985.6 |
| 11 | 286.8 | 1 | 1005.2 |
| 10 | 365.4 | 0 | 1013.0 |

### c. N-TbFlux algorithm

The computation of the fluxes by N-TbFlux is split into three steps. The first step consists of adding small biases, or $\delta$s, to the radiances' equivalent brightness temperatures (Tb). These corrections account both for possible fluctuations of the radiometric calibration, including the satellite changes, and for errors in the radiance forward calculations performed for the setting of the neural network parameters (the learning phase), including those errors from the solar radiation effect. The $\delta$ values are automatically computed at LMD from collocations between radiosonde reports and TOVS observations (Scott et al. 1999); they are based on a 3-month running mean of the differences between the observations and the computations. The $\delta$s are less than 0.5% of the Tb values and the corresponding standard deviations are small in comparison with these biases.

After the $\delta$ correction is made, N-TbFlux selects a neural network among 60. As in the 3I inversion scheme, N-TbFlux uses 10 reference angles for the satellite viewing angle, from nadir to 60°, 19 surface pressures, and two types of surface: land and sea. For the sea, only the pressure level $P_s = 1013$ hPa is used. Chaboureau (1997) showed that the Tb variations behave uniformly for adjoining viewing angles: by way of biases, the Tbs for 10 viewing angles can be referred to only three angles, with an error comparable to the instrument noise. Thus, to take into account three viewing angles, 19 surface pressures for land, and one for sea, N-TbFlux uses 60 different neural networks. For a given situation, N-TbFlux selects the one that deals with the viewing angle, and also the surface type and pressure, closest to the situation. The chosen neural network computes the vertical clear-sky LW flux profiles. The vertical grid on which the fluxes are estimated is presented in Table 1. The atmosphere is divided into 19 layers from TOA to 1013 hPa; the fluxes are estimated at the corresponding 20 pressure levels.

### d. Characteristics of the neural networks in N-TbFlux

The neural networks of N-TbFlux do not use all the available information of the TOVS observations. Some

TABLE 2. Main spectral characteristics of the HIRS channels.

| Channel | Central frequency ($\mu$m) | Central frequency ($cm^{-1}$) | Main absorbing gases | Max of the weight function (hPa) |
|---|---|---|---|---|
| H1 | 14.96 | 668.40 | $CO_2$ | 30 |
| H2 | 14.72 | 679.20 | $CO_2$ | 60 |
| H3 | 14.47 | 691.10 | $CO_2$ | 100 |
| H4 | 14.21 | 703.60 | $CO_2$ | 400 |
| H5 | 13.95 | 716.10 | $CO_2$ | 600 |
| H6 | 13.36 | 732.40 | $CO_2/H_2O$ | 800 |
| H7 | 13.36 | 748.30 | $CO_2/H_2O$ | 900 |
| H8 | 11.14 | 897.70 | Window/$H_2O$ | Surface |
| H9 | 9.73 | 1027.90 | $O_3$ | 25 |
| H10 | 8.22 | 1217.10 | $H_2O$ | 900 |
| H11 | 7.33 | 1363.70 | $H_2O$ | 700 |
| H12 | 6.74 | 1484.40 | $H_2O$ | 500 |
| H13 | 4.57 | 2190.40 | $N_2O$ | 1000 |
| H14 | 4.52 | 2212.60 | $N_2O$ | 950 |
| H15 | 4.46 | 2240.10 | $CO_2/N_2O$ | 700 |
| H16 | 4.40 | 2276.30 | $CO_2/N_2O$ | 400 |
| H17 | 4.24 | 2360.60 | $CO_2$ | 5 |
| H18 | 4.00 | 2512.00 | Window | Surface |
| H19 | 3.70 | 2671.80 | Window | Surface |
| H20 | 0.70 | 14 285.70 | Window | |

channels, which are useful for other applications, are less interesting for the computation of LW fluxes. The chosen inputs of the neural networks are HIRS temperature-sounding channels 2, 3, 4, 5, 6, 7, 13, 14, and 15; HIRS surface temperature–sounding channels 8 and 18; and HIRS water vapor–sounding channels 10, 11, and 12. The reader is referred to Table 2 for the main characteristics of the HIRS channels. These inputs can be either the observed Tbs or the corresponding cloud-cleared Tbs, both corrected with the $\delta$s. The cloud-cleared possibility is not used in the current study (see section 3b). The neural networks have 14 inputs (the 14 mentioned Tbs) and 40 outputs (the 20 upward fluxes and the 20 downward fluxes). The number of outputs is smaller in cases of elevated terrain.

The learning radiance datasets (inputs) for N-TbFlux are based on the Thermodynamic Initial Guess Retrieval (TIGR-3) databank (Achard 1991; Escobar-Munoz et al. 1993; Chevallier et al. 1998). For each of the 2300 atmospheric situations, the Automatized Atmospheric Absorption Atlas (4A) line-by-line radiative transfer model (Scott and Chédin 1981; Tournier et al. 1995) was used to compute the corresponding HIRS Tbs. The calculations were performed for the 10 viewing angles, the 19 pressure levels, and the two typical surface emissivities (sea and land). The spectral characteristics of the HIRS instrument are taken from the one aboard *NOAA-11*. The European Centre for Medium-Range Weather Forecasts (ECMWF) operational wideband model (Morcrette 1991; Zhong and Haigh 1995) was used to compute the vertical radiative flux profiles of the learning datasets (outputs) corresponding to the computed Tbs. It is planned to use a line-by-line model in the future.

TABLE 3. Mean ($m$) and standard deviation ($\sigma$) of the comparison between the computations of N-TbFlux from simulated TOVS Tbs and those of 4A from the corresponding geophysical parameters, on 1032 radiosonde reports: fluxes from N-TbFlux minus fluxes from 4A (W $m^{-2}$). Results are shown by airmass class. OLR: Outgoing Longwave Radiation. LSNF: LW Surface Net Flux. TLC: Total LW Cooling.

| Airmass class | OLR | | LSNF | | TLC | |
|---|---|---|---|---|---|---|
| | $m$ | $\sigma$ | $m$ | $\sigma$ | $m$ | $\sigma$ |
| Tropical | 1.0 | 1.2 | 1.0 | 10.7 | 0.0 | 10.5 |
| Midlatitude | 1.1 | 0.8 | −0.6 | 5.1 | 1.7 | 5.0 |
| Polar | 1.4 | 0.9 | 0.2 | 2.9 | 1.1 | 2.9 |

### *e. Error estimation*

N-TbFlux has been validated for synthetic cases, based on a dataset of 1032 radiosonde reports (Moulinier 1983). These observations cover a wide range of atmospheric situations all of which are different from those in the learning datasets. They have been classified into three statistically homogeneous airmass classes (Achard 1991; Chevallier et al. 1998): tropical (265 situations), midlatitude (509 situations), and polar (258 situations). The situations were described initially by the temperature, the water vapor, and the ozone profiles. As with the learning datasets, the 4A model has been used to simulate the corresponding Tbs, and the ECMWF wideband model was used to compute the vertical fluxes.

The computations of the fluxes by N-TbFlux from the Tbs are compared with the reference ECMWF wideband model computations. The results for the nadir view and the maritime surface are shown in Table 3 and Fig. 1. The cooling-rate reference computations are illustrated in Fig. 2. The differences are decomposed into a systematic error (the bias) and a random error (the standard deviation). Because some sources of error, such as the uncertainty about the HIRS filter functions, are not taken into account in this section, the results show a lower limit to actual accuracies but provide a qualitative estimation of the method.

The computed OLRs are biased by about 1.2 W $m^{-2}$, whatever the airmass class is. The corresponding standard deviations are less than 1.2 W $m^{-2}$. The error is larger for both LSNF and TLC, with a standard deviation ranging from about 11 W $m^{-2}$ in the tropical class to 3 W $m^{-2}$ in the polar one. The bias is less than 2 W $m^{-2}$. For cooling rates, the biases generally are smaller than 0.1 K $day^{-1}$. The standard deviations range from 0.1 to 0.4 K $day^{-1}$. Higher biases are found at 10 hPa because of a systematic overestimation of the vertical downward flux variations. The uncertainty of N-TbFlux for higher zenith angles is similar to those presented at nadir, except for LSNF and TLC in the tropical class, for which the standard deviation increases by about 1 W $m^{-2}$ (not shown).

The results for OLR and the vertical cooling rates are

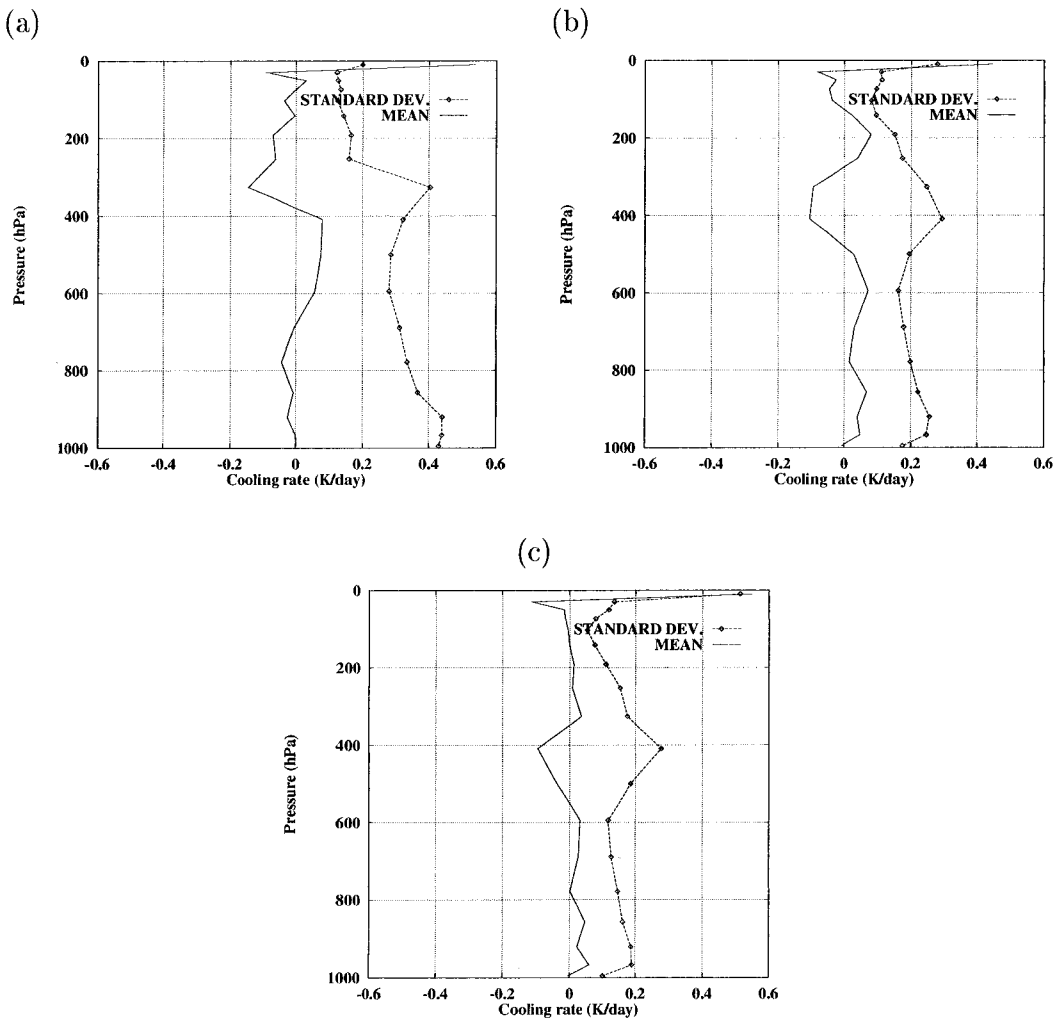


FIG. 1. Comparison between the computations of N-TbFlux from simulated TOVS Tbs and 4A from the corresponding geophysical parameters on 1032 radiosonde reports [cooling rates from N-TbFlux minus cooling rates from 4A (K day$^{-1}$)]. Results are shown by airmass class: (a) tropical, (b) midlatitude, and (c) polar.

comparable to the spread of the computations from various radiative transfer models used in GCMs (Ellingson and Ellis 1991; Baer et al. 1996). Recall that models such as the ECMWF one or the 4A line-by-line model use the geophysical description of the atmosphere to compute the fluxes. Under clear conditions, the models tested by Baer et al. give cooling-rate profiles varying from one another by about 0.5 K day$^{-1}$ at most pressure levels. Because the current validation uses synthetic cases and not real observations, it does not investigate two aspects of N-TbFlux: the $\delta$ correction and the accuracy of the radiative transfer model (RTM) used in the learning datasets to compute the reference fluxes (here the ECMWF wideband model). The $\delta$ correction is taken into account in sections 5 and 6. As far as RTM is concerned, Chevallier et al. (1998) showed on a similar problem that the neural network method can simulate at a given speed any RTM, including line-by-line ones, with the same accuracy as that RTM. The possibility of using a line-by-line RTM for N-TbFlux has not been investigated yet, but the results therefore are expected to be similar to those presented here.

The high values of the computed LSNF error for N-TbFlux probably are related to the poor vertical resolution of HIRS in the lower atmosphere rather than to a limitation of the neural network–based approach. Indeed, according to Gupta (1989), 86% of the downward radiation arriving at the surface comes from the lower 50-hPa layer, and the sensitivity of the HIRS channels to such an atmospheric layer is known to be weak. That is why previous studies with different fast methods also reported high uncertainty in the estimation of the downward LW fluxes at the surface; Gupta et al. (1992) show an uncertainty of about 20 W m$^{-2}$, and Ellingson et al. (1994) report an error of about 10 W m$^{-2}$.

+3,650/351-,5/.8(4734,./. !"#"! $%##&)+*

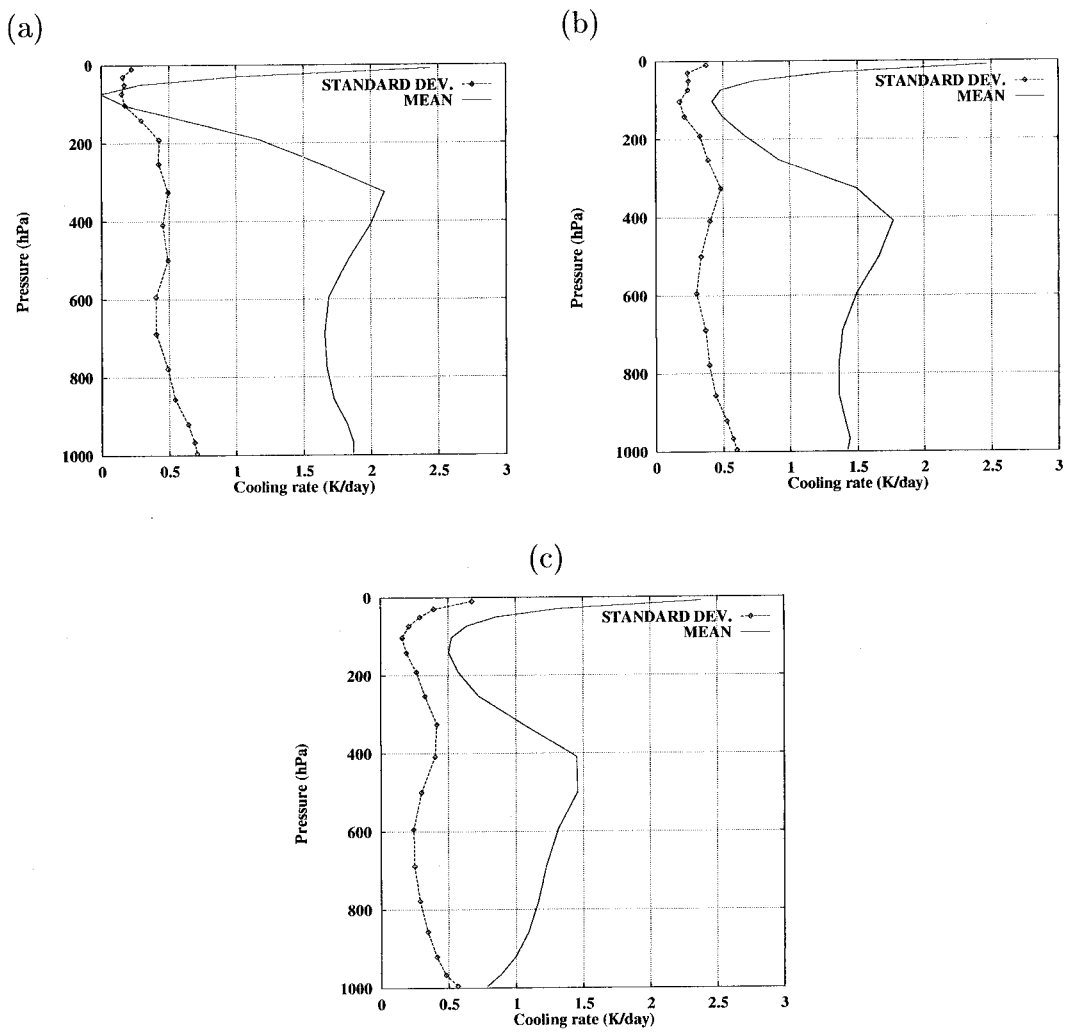


FIG. 2. Mean and standard deviation of the cooling rates computed by the ECMWF wideband model on the 1032 radiosonde reports (K day$^{-1}$). Results are shown by airmass class: (a) tropical, (b) midlatitude, and (c) polar.

## 4. Flux retrieval from 3I-retrieved geophysical properties

### *a. 3IFlux algorithm*

Apart from the statistical methods to which N-TbFlux belongs, other techniques have been developed to infer radiative fluxes from TOVS observations. They successively use a retrieval scheme to obtain the geophysical properties from the Tbs and a radiative transfer forward model to compute the fluxes (e.g., Darnell et al. 1986; Zhang et al. 1995; Mehta and Susskind 1999).

This approach also has been explored at LMD (Chéruy et al. 1994, 1996b). The latter method (3IFlux) uses the 3I retrieval product, an interface, and the ECMWF wideband radiative transfer model.

The retrieval of certain cloud properties viewed from the top of the atmosphere is made possible by the TOVS spectral characteristics: effective cloud emissivity, cloud-top pressure, and cloud-top temperature (Stubenrauch et al. 1999b). The estimation of the vertical full-sky LW fluxes from TOA to the surface (Chéruy et al. 1996b) requires the completion of the information contained in the TOVS radiances with a climate dataset such as the one from Poore et al. (1995). This weakness prohibits the vertical heterogeneities of the clouds from being taken into account and induces great uncertainties in the vertical radiative fluxes estimations, especially in the downward ones. The resulting estimation of the full-sky LW radiative cooling rates is particularly difficult to analyze. Therefore, the current study has been restricted to the estimation of the clear-sky contribution to the fluxes and cooling rates, a subject about which critical questions currently are being studied.

### *b. The 3I-retrieved variables*

The 3I retrieval method is a physico-statistical scheme dedicated to retrieval of atmospheric, cloud, and

surface parameters (Chédin et al. 1985; Scott et al. 1999). It makes use of the TIGR databank in which a first solution to the inversion is selected by a pattern recognition approach.

Within the framework of the NOAA/National Aeronautics and Space Agency (NASA) Pathfinder program, 8 yr of TOVS data (*NOAA-10* and *NOAA-12*) already have been processed by the 3I algorithm. The 3I–Pathfinder data are organized in a 1° lat × 1° long grid. Temperature profiles, originally retrieved for 28 pressure layers from 1013 to 10 hPa, are archived on a nine-layer vertical grid. The layers are bounded by the following standard pressure levels: the surface, and 850, 700, 500, 300, 100, 70, 50, 30, and 10 hPa. This pressure grid was chosen according to the performances of the TOVS sounder, which were issued from its specifications. For instance, in a data assimilation context, Thépaut and Moll (1990) showed that the use of HIRS and MSU observations provides no more than seven independent statistical pieces of information for the temperature and water vapor. Chevallier (1998) confirmed that, for the current study, the restriction from 28 to nine layers for the temperature description does not significantly affect the results. The vertical distribution of water vapor appears in the 3I–Pathfinder dataset under the form of integrated quantities over five layers bounded by levels at the surface and at 850, 700, 500, 300, and 100 hPa (Chaboureau et al. 1998). The characteristics of the clouds (effective cloud emissivity, cloud-top pressure and temperature, and cloud type) also are retrieved (Stubenrauch et al. 1999b). All these quantities are available in the 3I–Pathfinder dataset on a daily, 5-day (pentad), and monthly basis, for the morning (AM) and the evening (PM) overpasses of the satellite.

### c. From the 3I-retrieved variables to the radiative transfer model

The LW flux profiles corresponding to the 3I-retrieved geophysical parameters are obtained by applying the ECMWF wideband radiative code, which is used also for the setting of N-TbFlux parameters. For a particular atmospheric situation (clear as well as cloudy), the radiative transfer model computes both the clear and the cloudy components of the LW flux profiles. The main inputs required for the computation of the clear-sky component are the temperature, water vapor, and ozone profiles and the surface temperature. Most of these quantities are available from the 3I outputs after some postprocessing. For water vapor, a crude assumption has to be made to estimate the mixing ratio vertical profile from the 3I-integrated quantities; in the current study, it is assumed that the relative humidity does not change inside the five retrieval layers. This assumption is discussed in section 4e. The ozone profile, which is not retrieved here from TOVS, comes from the climate dataset of McPeters et al. (1984). For a better estimation of the vertical integrals in the radiative computations, the vertical resolution of the atmospheric profiles has been increased by interpolation from the nine 3I–Pathfinder layers to the 19 layers from Table 1.

This process for the estimation of the LW fluxes from TOVS requires that the 3I algorithm succeed in retrieving all the needed parameters from the TOVS Tbs: the temperature and water vapor profiles, and the surface temperature. Chaboureau (1997) indicates that all the needed parameters are retrieved for about 90% of the clear-sky data, but this score decreases to about 75% for the partly cloudy situations and to about 10% for the overcast ones. For overcast situations, the 3I retrieval scheme rejects the data when there is more than 60% cloudiness on each HIRS pixel within the retrieval grid box. These gaps have not been filled.

### d. Computed quantities

Because the water vapor profiles used in the forward radiative transfer computations come from only five coarse layers, the 19 layers shown in Table 1 obtained from interpolation do not give additional information on the vertical thermodynamic structure of the atmosphere. Thus, the 3IFlux cooling rates have been averaged on six coarse layers. The pressure levels at the boundaries are the surface, and 950, 850, 500, 300, 100, and 0 hPa. They correspond approximately to the water vapor layers. The two layers 850–700 hPa and 700–500 hPa have been merged. The 3I–Pathfinder surface–850 hPa layer has been divided into two sublayers to take into account, over the oceans, the dominating influence of the surface temperature in the boundary layer.

### e. Sensitivity studies to input data uncertainties

To estimate the accuracy of the fluxes computed from 3IFlux, a series of sensitivity tests were performed. These tests consist in perturbing the geophysical variables used as inputs to the ECMWF radiative code rather than perturbing the Tbs, as was done for N-TbFlux validation. This method indirectly enables the uncertainty in the $\delta$ computation, used by 3I as well as by N-TbFlux, to be taken into account. The values of the perturbations have been chosen to be of the same order of magnitude as the differences observed (plus or minus one standard deviation) between 3I-retrieved temperature or water vapor profiles and radiosonde measurements of the same quantities (Scott et al. 1999). The authors are aware that because of the irregular spread of the radiosoundings, some kinds of errors may be poorly documented. The estimated uncertainties in the temperature profiles are about 2.0 K in the higher and lower atmosphere and about 1.5 K in the middle atmosphere. For the water vapor, they reach 40% in the 500–300-hPa layer and decrease to about 25% in the 1013–850-hPa layer. These numbers refer to standard deviations, because the retrieved quantities are nearly unbiased. Because of its effect on infrared radiation, cloudiness is the major fac-

TABLE 4. Global mean ($m$) change and associated standard deviation ($\sigma$) in monthly mean fluxes (W m$^{-2}$) produced by successively perturbing the input variables by the amount indicated in section 4e: temperature, water vapor, and then surface temperature.

| | OLR | | LSNF | | TLC | |
|---|---|---|---|---|---|---|
| Perturbed parameter | $m$ | $\sigma$ | $m$ | $\sigma$ | $m$ | $\sigma$ |
| Temperature | 7.6 | 1.7 | −2.9 | 2.2 | 10.6 | 2.8 |
| Water vapor | −4.1 | 2.1 | −12.5 | 5.9 | 8.3 | 4.1 |
| Surface temperature | 3.9 | 1.3 | 10.7 | 1.5 | −6.8 | 2.2 |

tor of error in the 3I-retrieved temperature and water vapor profiles. As a consequence, the cloudiness has an effect on the quality of the 3IFlux flux estimation, even though these fluxes are clear ones. In the radiosonde reports used in the 3I validation [the so-called DSD5 archive from NOAA National Environmental Satellite Data and Information Service (NESDIS); Uddstrom and McMillin 1993], the surface bulk temperature has been recorded but not the surface skin temperature. Therefore, the 3I-retrieved surface skin temperature has been validated against monthly means of sea surface temperature from the Advanced Very High Resolution Radiometer (AVHRR) Pathfinder analyses. No detailed 3I validation statistics over land yet exist. Consequently, in the current study, a rough estimation of the skin surface temperature uncertainty of 2.0 K standard deviation over the land and 1.5 K over the sea was used.

Two months have been processed for these sensitivity tests: January 1988 and July 1988. Because results are similar for the two months, only those results from January 1988 will be considered here. They are shown in Table 4 for OLR, LSNF, and TLC and on Fig. 3 for the cooling rates. Computations obtained with negative perturbations (minus one error standard deviation) have been subtracted from the ones obtained with positive perturbations (plus one error standard deviation).

The observed means for the cooling rates can be explained by simple considerations on the radiative transfer. When the water vapor concentration is decreased, both the emission and the absorption of the atmosphere decrease. The radiation emission decrease has a dominating influence, as illustrated in Table 4 in which the surface downward flux increase is shown to be larger than the OLR decrease. Therefore the overall cooling decreases and the mean difference in cooling rate is positive on the whole column (Fig. 3b). When one decreases the surface temperature instead of the water vapor, the radiative heating of the lower atmosphere decreases (Fig. 3c). When one decreases the atmospheric temperature, there are two opposite effects; in the lower atmospheric layer, the effect is similar to a decrease of the surface temperature, whereas, in the other layers, the effect is to decrease the Planck emission and thus the cooling (Fig. 3a). The signs of the OLR and LSNF variations can be explained in a similar manner. From these considerations, it can be seen that the values presented here are only rough estimations of the uncertainty in the computed LW radiative components. When all the input parameters are allowed to vary, individual changes may cumulate or compensate each other. Nevertheless, because the different calculations are self consistent, the errors from the various geophysical parameters are correlated and are expected to compensate more than to accumulate.

Uncertainty in the OLR is dominated by the atmospheric temperature influence, which represents about twice that of the surface temperature or water vapor. The accuracy of LSNF is highly dependent on the accuracy of the water vapor and surface temperature retrievals, whereas low sensitivity to atmospheric temperature uncertainty is shown. For TLC, the sensitivities to atmospheric temperature, water vapor, and surface temperature are similarly important because of mutual cancellations between the TLC components. These numbers are consistent with the Zhang et al. study (1995), although the latter took the cloud radiative forcing into account.

For radiative cooling rates (Fig. 3), the dominant influence of the surface temperature in the first, lowest layer can be noticed, with a systematic change of 0.6 K day$^{-1}$. The weak standard deviation is due to the rough estimation of the surface temperature uncertainty and therefore may be underestimated. From 950 to 850 hPa, the atmospheric temperature has the strongest influence, with a mean change of 0.3 K day$^{-1}$ and a standard deviation of the same magnitude. In the 850–300-hPa layers, the cooling rates are equally sensitive to atmospheric temperature and water vapor uncertainties, with means and standard deviations near 0.1 K day$^{-1}$. The layers above 300 hPa are dominated by atmospheric temperature uncertainties, with a mean of up to 0.2 K day$^{-1}$.

The influence of the assumption made for estimating the water vapor mixing ratio from the 3I-retrieved layered water vapor contents also has been evaluated. The fluxes and cooling rates associated with 1032 radiosondes from Moulinier (1983) have been computed with and without assuming that the relative humidity is constant in each layer. In comparison with the other uncertainties, the effect appears to be negligible on OLR, LSNF, and TLC: the means and standard deviations of the difference are below 1 W m$^{-2}$. For cooling rates, biases are below 0.1 K day$^{-1}$ between 1013 and 300 hPa, but range between 0.1 and 0.2 K day$^{-1}$ for pressure levels above 300 hPa. Standard deviations are below 0.2 K day$^{-1}$ (figure not shown). It is obvious that these

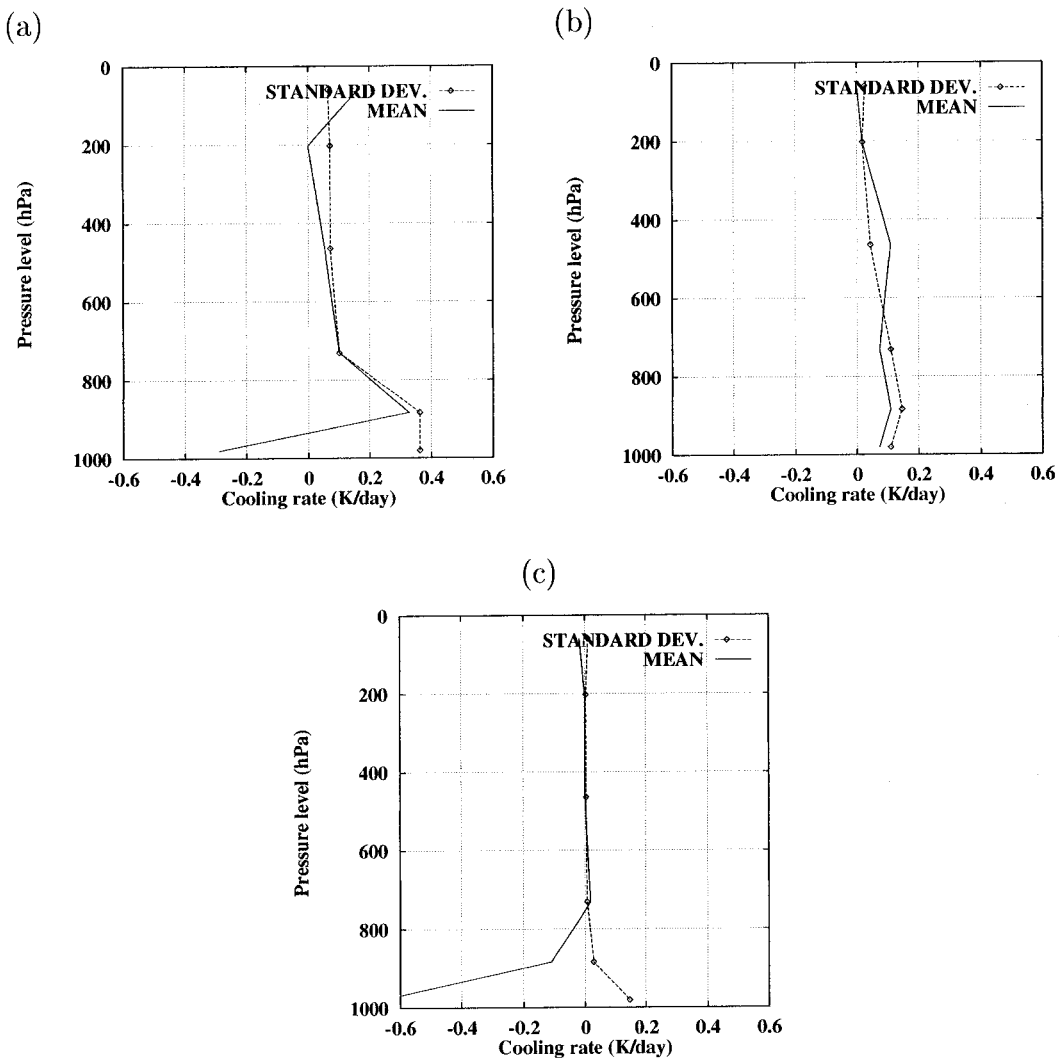


FIG. 3. Global mean change and associated standard deviation in monthly mean cooling rates (K day$^{-1}$) produced by changing the input variables to the radiative transfer model by the amount indicated in the text: (a) temperature only, (b) water vapor only, and (c) surface temperature only.

errors are not correlated with the previous ones but rather add to them. Nevertheless, as the values of the fluxes, and of the cooling rates between the 300-hPa level and the surface, are nearly unbiased, the crude assumption relating to water vapor should not affect the climatological signals of these variables.

## 5. Comparisons of computed fluxes based on radiosonde reports

A comparison has been made between flux computations from N-TbFlux, from 3IFlux, and from direct computations with the ECMWF wideband model using radiosonde archives from NOAA/NESDIS (the DSD5 archive; Uddstrom and McMillin 1993) currently used at LMD for validation of the 3I-retrieved variables. The current study uses the *NOAA-10* collocation files from September 1987 to October 1989 restricted to oceanic areas and to clear-sky conditions, as determined by the 3I retrieval method. Eight-hundred and thirteen satellite–radiosonde collocated situations were found matching this criterium, 756 of which had all the needed 3I-retrieved geophysical variables. Recall that the changes in spectral characteristics from *NOAA-11* to *NOAA-10* are taken into account in both 3I and N-TbFlux by the $\delta$s (see section 3c).

The radiosonde-based computations will be viewed as the reference computations. One has to keep in mind, however, the uncertainties induced by the radiosonde measurements (e.g., McMillin et al. 1992; Luers and Eskridge 1998) and by the collocation window (100 km, 3 h). Moreover, as was said before, the surface skin temperature has not been archived in the DSD5 files. In the present computations, the sea surface temperature

+3,650/351-,5/.8(4734,./. !"#"! $%##&)+*

TABLE 5. Mean ($m$) and standard deviation ($\sigma$) of the comparison between the computations of N-TbFlux and 3IFlux from observed TOVS Tbs and those of the ECMWF wideband model from collocated radiosonde soundings: fluxes from either N-TbFlux or 3IFlux minus fluxes from the reference computation (W m$^{-2}$). In the case of cloudiness, the cloud radiative forcing on the LW fluxes is not taken into account.

| Sky condition | Method | No. of situations | OLR | | LSNF | | TLC | |
|---|---|---|---|---|---|---|---|---|
| | | | $m$ | $\sigma$ | $m$ | $\sigma$ | $m$ | $\sigma$ |
| Clear skies | N-TbFlux | 813 | −0.9 | 9.6 | −1.4 | 11.5 | 0.5 | 14.1 |
| Clear skies | 3IFlux | 756 | 1.1 | 10.7 | 7.0 | 13.6 | −5.9 | 15.0 |
| All skies | 3IFlux | 6052 | −0.3 | 9.4 | 4.0 | 13.6 | −4.3 | 13.2 |

from the National Centers for Environmental Prediction analyses has been used. This merging of two different datasets may be responsible for the significant uncertainty in the fluxes at the surface and therefore in the cooling rates in the lower atmosphere. Also, the water vapor profiles have been extrapolated above their respective highest measurement level.

Table 5 displays the results for OLR, LSNF, and TLC. Small biases are observed for OLR: 0.9 W m$^{-2}$ for N-TbFlux and 1.1 W m$^{-2}$ for 3IFlux. The standard deviations are much higher: about 10 W m$^{-2}$ for both methods. A large degradation of N-Tbflux accuracy, as deduced from Table 3, is observed. This degradation may be due both to the uncertainty caused by the $\delta$s, which could not be taken into account in the previous experiment, and to the uncertainties in the geophysical parameters used in the reference computation. The second point also applies to 3IFlux and is likely to explain the high standard deviation. Results of N-TbFlux and 3IFlux for LSNF and TLC are comparable for standard deviations: between 10 and 15 W m$^{-2}$. The corresponding absolute biases are less than 1.5 W m$^{-2}$ for N-TbFlux, but exceed 6 W m$^{-2}$ for 3IFlux. Nevertheless, the previous remark on the reference fluxes at the surface makes these numbers difficult to interpret.

The statistics for the cooling rates are shown in Figs. 4a (N-TbFlux) and 4b (3IFlux). For consistency between the results of N-TbFlux and those of 3IFlux, the statistics are presented with the reduced vertical discretization from section 4d. Biases between N-TbFlux and the radiosonde-derived computations are less than 0.15 K day$^{-1}$. The corresponding standard deviation regularly increases from 0.1 K day$^{-1}$ for the highest layer to 0.5 K day$^{-1}$ for the lowest one, which is comparable to the estimations from Fig. 1. The standard deviations observed between 3IFlux and the reference computations are similar, but absolute biases of 0.2 K day$^{-1}$ in the 300–500-hPa layer and of 0.4 K day$^{-1}$ in the lower layer can be noted. Again, the results in the 950–1013-hPa layer are very uncertain, because the corresponding cooling rates are influenced highly by the surface temperature.

This study has been extended to all sky situations. In the case of cloudiness, 3IFlux uses the atmospheric and surface parameters retrieved from 3I cloud-cleared radiances. Recall that only 3IFlux can be used in cases of cloudiness because of the version of the 3I algorithm that is used for the decontamination of the radiances from the influence of clouds (see section 3b). Results are presented in Table 5 and Fig. 4c. They are comparable to those for clear-sky situations only. They show even better agreement between the 3I-derived fluxes and the reference ones. For instance, the bias for the net flux at the surface amounts to 4 W m$^{-2}$. These comparisons with radiosonde-based computations tend to confirm the previous estimations of the accuracy of the two methods.

## 6. OLR comparisons with ERBE observations

### *a. The ERBE data*

The ERBE experiment has provided one of the most complete and accurate datasets on radiative fluxes at TOA. It was designed as a system of three satellites, two of which belong to the NOAA series: *NOAA-9* and *NOAA-10*. Thus, together with TOVS and AVHRR, the ERBE instruments were flown on these two satellites, allowing comparisons between the instantaneous estimations of OLR from TOVS and from ERBE (ERBE S8 product). For practical reasons, in many studies of OLR (e.g., Slingo et al. 1998; Mehta and Susskind 1999) comparisons are made against the ERBE monthly mean product instead of the ERBE instantaneous one. Although of recognized usefulness, the monthly mean product includes various processings that makes it prone to cloud contamination (Slingo and Webb 1992) and a tendency toward the sampling of the drier profiles (Allan et al. 1999). Therefore all comparisons presented in the following use the ERBE instantaneous values.

The conversion from the measured radiances of the ERBE scanners to OLR estimations, via spectral and angular correction (Smith et al. 1986), induces considerable uncertainties in the OLR estimations. The instantaneous pixel error standard deviation for all-sky OLR has been estimated to be as large as 12.7 W m$^{-2}$ (Wielicki et al. 1995). Because of error compensations, the widely used monthly mean products (ERBE S9) display a smaller uncertainty: 3.2 W m$^{-2}$. For the clear-sky situations only, various estimates (e.g., Harrison et al. 1990; Hartmann and Doelling 1991; Hartmann et al. 1992; Collins and Inamdar 1995; Slingo et al. 1998) agree with the existence of biases in the ERBE OLRs, ranging between 2 and 6 W m$^{-2}$, and even higher in particular conditions such as deep convective activity.

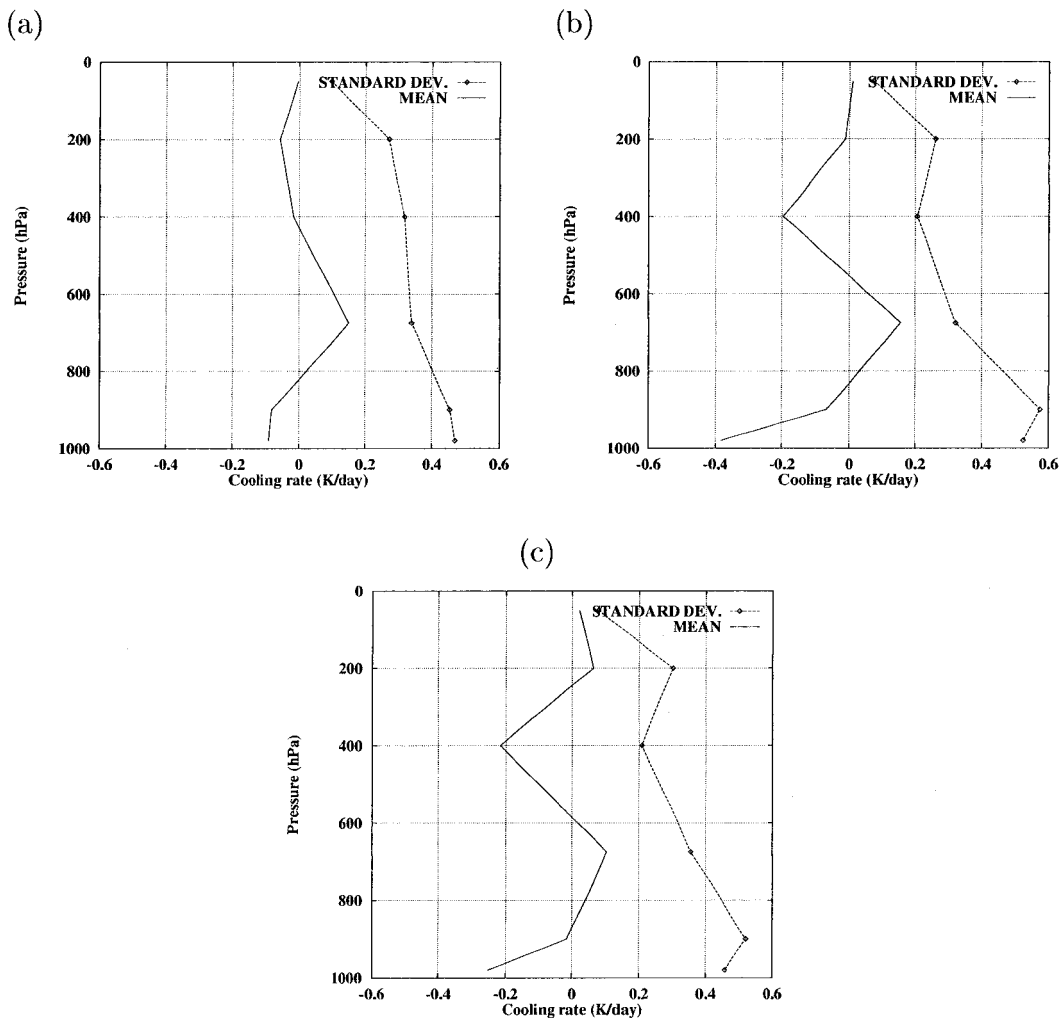


FIG. 4. (a) Comparison between the computations of N-TbFlux and the computations from radiosonde observations for clear-sky situations: cooling rates from N-TbFlux minus reference cooling rates (K day$^{-1}$). (b) As in (a) but with 3IFlux. (c) As in (b) but for all sky situations, although the cloud radiative forcing on the LW fluxes is not taken into account.

*b. Results of the comparisons*

For the current study, 4 months of *NOAA-10* data have been time–space collocated (Stubenrauch et al. 1999c): July 1987, October 1987, January 1988, and April 1988. To ensure accurate spatial collocation, the ERBE coordinates given at TOA are transformed into surface coordinates that are used in the 3I dataset. This study is restricted to conditions thought actually to be clear. The statistics between clear-sky OLR derived from ERBE and OLR computed by N-TbFlux (respectively, 3IFlux) are shown in Table 6 (respectively, Table 7). The determination of clear sky comes from the 3I retrieval model. Land and sea geotypes are considered separately for the whole globe, both in the morning (about 0730 local time) and then in the evening (about 1930 local time) overpasses of the satellite. The numbers of collocated situations from the two sets (N-TbFlux and 3IFlux) are not the same, because 3IFlux uses 1° × 1° gridding, and N-TbFlux works on 100-km × 100-km regions. It can be seen that the magnitude of the differences is comparable to the uncertainties in the instantaneous fluxes from N-TbFlux, 3IFlux, and ERBE. The standard deviations with ERBE (about 6 W m$^{-2}$) are similar for N-TbFlux and 3IFlux. The biases obtained with 3IFlux do not exceed 5 W m$^{-2}$. They can differ from those of N-TbFlux, which are less than 4 W m$^{-2}$, by up to 4 W m$^{-2}$. On average, OLRs computed by the two methods explain more than 98% of the variance in the ERBE dataset.

To sharpen the analysis, the study has been focused on the evening overpasses (PM) of October 1987. Figure 5 shows the differences between the computed OLR and the ERBE determination as a function of surface temperature for the open sea and the land geotypes. The

TABLE 6. Statistics from the comparison between ERBE OLR and the computations of N-TbFlux: OLR (computed) − OLR (ERBE) (W m$^{-2}$). *NOAA-10*, clear sky identified by the 3I retrieval scheme.

| Year | Month | Over-path | Geotype | No. of situations | Bias | Std dev | Correlation |
|---|---|---|---|---|---|---|---|
| 1987 | 07 | AM | Ocean | 30 545 | 2.2 | 4.7 | 0.992 |
| | | | Land | 42 406 | 1.4 | 6.5 | 0.969 |
| | | PM | Ocean | 37 366 | 1.0 | 5.3 | 0.988 |
| | | | Land | 33 651 | 0.9 | 7.3 | 0.967 |
| 1987 | 10 | AM | Ocean | 31 541 | −0.9 | 5.2 | 0.989 |
| | | | Land | 45 843 | −1.5 | 6.6 | 0.982 |
| | | PM | Ocean | 36 280 | 1.2 | 5.6 | 0.985 |
| | | | Land | 35 032 | 2.6 | 6.3 | 0.985 |
| 1988 | 01 | AM | Ocean | 29 972 | −0.1 | 5.9 | 0.994 |
| | | | Land | 27 165 | −1.2 | 6.1 | 0.992 |
| | | PM | Ocean | 44 870 | 1.1 | 5.7 | 0.993 |
| | | | Land | 25 190 | 1.7 | 6.8 | 0.992 |
| 1988 | 04 | AM | Ocean | 44 037 | 1.5 | 5.6 | 0.993 |
| | | | Land | 39 768 | 1.3 | 6.8 | 0.985 |
| | | PM | Ocean | 48 943 | 2.3 | 5.7 | 0.993 |
| | | | Land | 27 674 | 3.5 | 6.5 | 0.985 |

TABLE 7. Same as Table 6 but for 3IFlux.

| Year | Month | Over-path | Geotype | No. of situations | Bias | Std dev | Correlation |
|---|---|---|---|---|---|---|---|
| 1987 | 07 | AM | Ocean | 21 957 | −1.0 | 5.9 | 0.982 |
| | | | Land | 26 612 | 4.7 | 7.5 | 0.948 |
| | | PM | Ocean | 27 384 | −1.6 | 6.4 | 0.973 |
| | | | Land | 19 556 | 3.6 | 7.5 | 0.941 |
| 1987 | 10 | AM | Ocean | 22 532 | −3.0 | 6.1 | 0.979 |
| | | | Land | 28 415 | −1.1 | 6.3 | 0.972 |
| | | PM | Ocean | 22 244 | 1.1 | 6.5 | 0.973 |
| | | | Land | 14 901 | 2.5 | 6.6 | 0.981 |
| 1988 | 01 | AM | Ocean | 21 983 | −4.1 | 7.0 | 0.990 |
| | | | Land | 17 191 | −3.4 | 6.3 | 0.988 |
| | | PM | Ocean | 33 264 | −1.8 | 6.3 | 0.987 |
| | | | Land | 11 932 | 1.3 | 6.7 | 0.993 |
| 1988 | 04 | AM | Ocean | 31 717 | −1.4 | 7.8 | 0.989 |
| | | | Land | 22 427 | −0.1 | 7.9 | 0.974 |
| | | PM | Ocean | 33 997 | −0.0 | 7.6 | 0.987 |
| | | | Land | 13 328 | 2.3 | 7.2 | 0.980 |

biases and standard deviations with ERBE are similar: biases of about 5 W m$^{-2}$ are found for surface temperatures lower than 15°C, and smaller ones are found for higher surface temperatures. Figure 6 shows the differences as a function of the atmospheric total water vapor content. They also are amazingly similar, though important differences remain between the two methodologies. Situations for which the water vapor content is lower than 0.3 cm are distinguished by an important spread of the various OLR determinations: the bias between N-TbFlux and ERBE reaches 20 W m$^{-2}$, whereas the standard deviation between 3IFlux and ERBE exceeds 30 W m$^{-2}$. This spread may point at a deficiency in the approach of 3IFlux, and of N-TbFlux to a smaller extent, that we analyze in the next section. More strik-

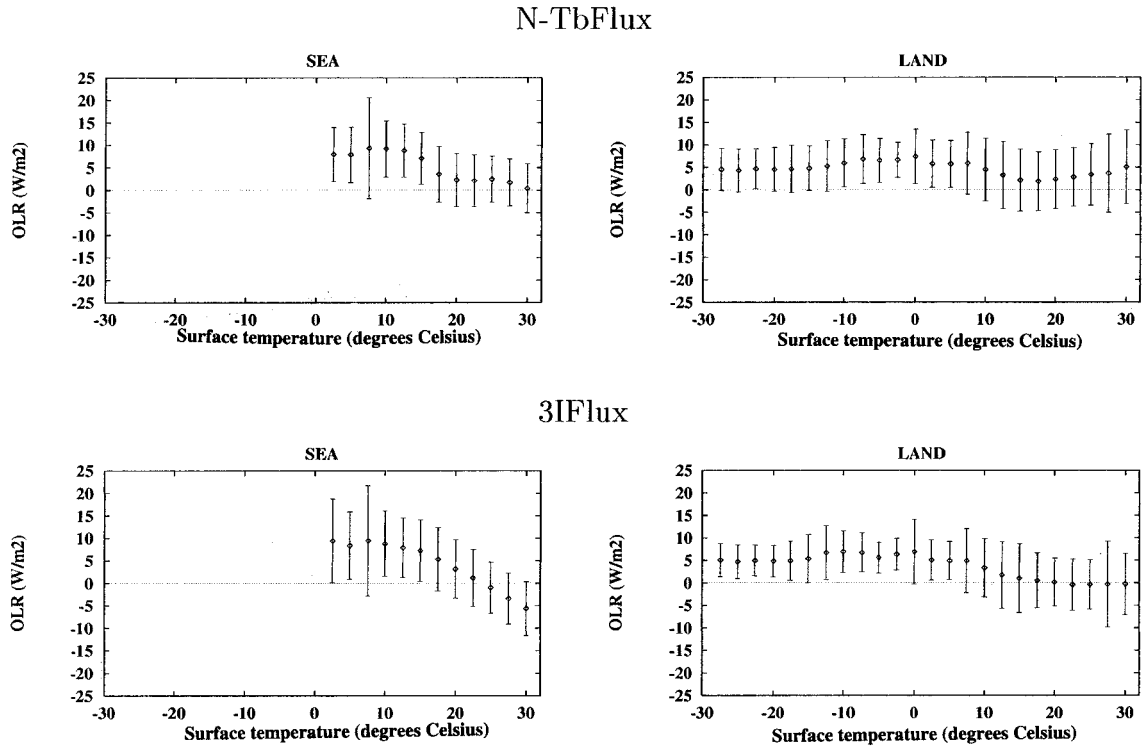


FIG. 5. Comparison between OLR measured by ERBE and the computations of N-TbFlux (top) and 3IFlux (bottom), as a function of surface temperature: OLR (computed) − OLR (ERBE) (W m$^{-2}$). Oct 1987, *NOAA-10* PM, clear skies. The definition of clear sky and the surface temperature come from the 3I retrieval scheme. The vertical bars represent the standard deviations. The horizontal scale is restricted to values between −30°C and +30°C.

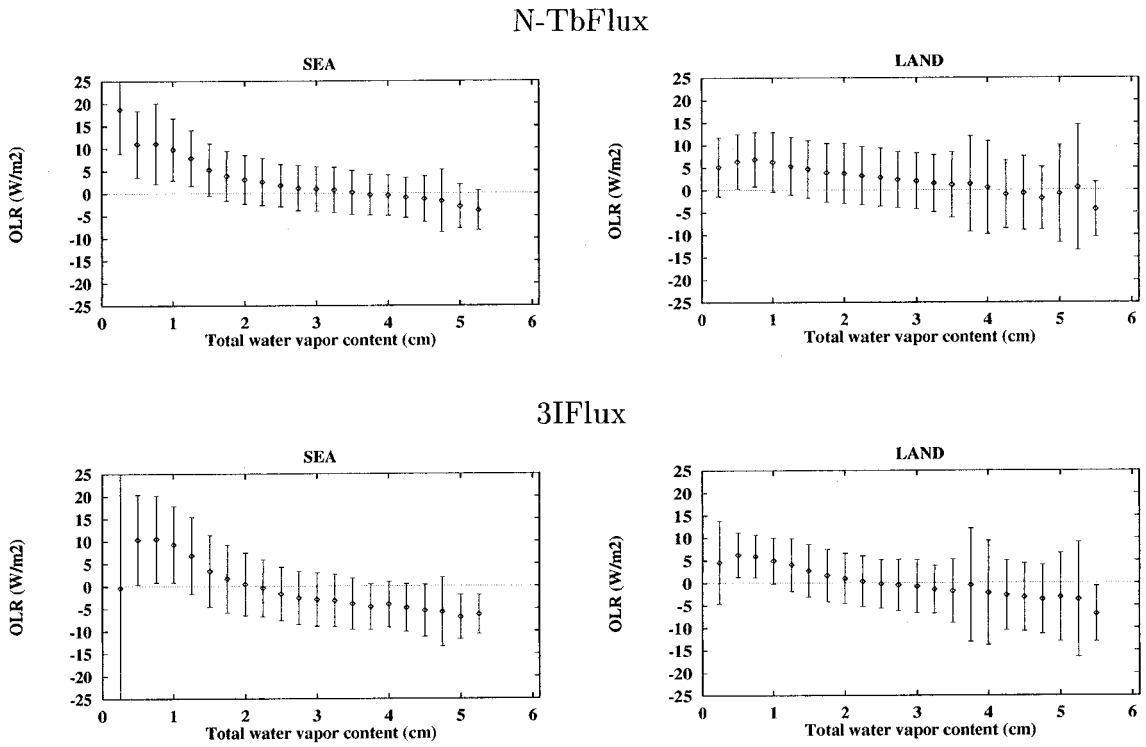


FIG. 6. As in Fig. 5 but the difference is expressed as a function of total water vapor content. The definition of the total water vapor content comes from the 3I retrieval scheme. The standard deviation for 3IFlux over the sea (left, bottom) for contents smaller than 0.3 cm reaches 32.7 W $m^{-2}$.

ing, both methods are characterized by a marked trend, with positive biases for small water vapor contents and negative biases for large contents. This trend appears at any latitude throughout the 4 months (result not shown). This trend is not observed in the previous radiosonde-based comparisons (result not shown).

The common features of N-TbFlux and 3IFlux that may explain such behavior are the use of the $\delta$s and the use of the ECMWF wideband model. For the $\delta$s, such an obvious water vapor–dependent estimation error is unlikely, because it also would have affected the 3I retrievals and appeared in the 3I validation. According to its validation against line-by-line computations (Chevallier 1998), the effect of the high level of parameterization of the ECMWF code on its accuracy should be limited to 2 W $m^{-2}$, if one admits that the current water vapor continuum modelizations are accurate. Similar tendencies between computed OLR and ERBE OLR, as a function of total water vapor content, have been observed by several authors: Collins and Inamdar (1995), using radiosonde data, and Slingo et al. (1998), using the ECMWF meteorological analysis. The ERBE S8 processing may be responsible for this effect. The measured ERBE radiances followed two processes; the first one corrected them from the spectral filter effects, and the second one converted them into fluxes (Smith et al. 1986). Because the trend also is apparent when looking at the corrected radiances (results not shown), the spectral correction should be the only cause of the problem.

To conclude, with the exception of situations for which water vapor content is lower than 0.3 cm, OLR computed by N-TbFlux and 3IFlux are characterized by an uncertainty that is comparable to that of the ERBE instantaneous product.

### *c. Use of SSM/I data in the 3IFlux process*

The deficiency of both 3IFlux and N-TbFlux for low water vapor contents is likely to be linked with the characteristics of the TOVS instrument. Indeed, infrared sounding is limited by known weaknesses induced by the form of the radiative transfer equation at the corresponding wavenumbers; when the contrast between the surface skin temperature and the temperature of the lower atmosphere is low, there is no sharp infrared weighting function that peaks in the boundary layer (e.g., Chéruy et al. 1995). This case is true for HIRS: too-humid retrievals of precipitable water have been observed in the subtropical maritime stratocumulus regions off the coast of California, Chili, Mauritania, and Angola (Stephens et al. 1994; Chaboureau et al. 1998), over which the vertical lapse rate is chiefly low. Atmospheric water vapor observations from satellite passive microwave imagers such as, for instance, Special Sensor Microwave Imager (SSM/I) on board of the De-

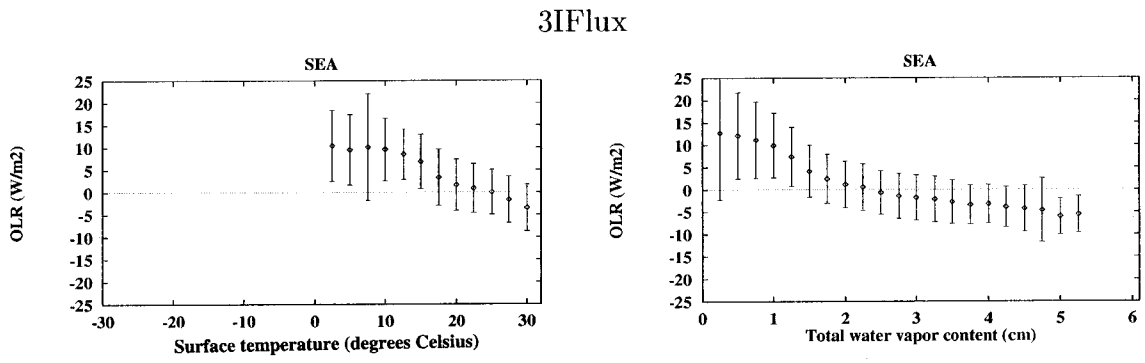


FIG. 7. Comparison between OLR measured by ERBE and the computations of 3IFlux, as a function of surface temperature (left) and total water vapor content (right): OLR (computed) − OLR (ERBE) (W m$^{-2}$). The SSM/I data are used in the 3IFlux process (see section 6c). Oct 1987, *NOAA-10* PM, clear skies. The definitions of clear-sky, surface temperature, and total water vapor content come from the 3I retrieval scheme. The vertical bars represent the standard deviations.

fense Meteorological Satellite Program (DMSP) series, suffer from different drawbacks: their measurements are exploitable only over open seas, their accuracy is lowered in cases of heavy rain, and the information from them does not yet allow the retrieval of the water vapor vertical distribution. TOVS, with both the HIRS and MSU instruments, illustrates the complementarity of both sounder types: infrared and microwave. On board of the *NOAA-15* platform, MSU, with only four channels near 50 GHz, was replaced recently by an Advanced MSU (AMSU) that groups the 15 channels of AMSU-A and the five channels of AMSU-B. This grouping will improve the quality of the water vapor retrievals, but, for the data previous to the availability of AMSU, the known failures of TOVS water vapor retrievals have to be taken into account.

An experiment has been conducted that studies the introduction of information from SSM/I in the 3IFlux process. Retrievals of total water vapor content from the SSM/I data over open sea with the algorithm from Alishouse et al. (1990) have been used. Because the NOAA and DMSP platforms are barely collocated in space and time, the monthly means of the total water vapor contents retrieved by the two methods have been computed and compared on the 3I-Pathfinder 1° × 1° grid. As said before, the low sensitivity of HIRS to water vapor in the lower atmosphere is a major source of difference. Among the other sources is the different number of points used for the computation of the monthly means. With only the poor vertical resolution being taken into account, the 3I total contents were adjusted by way of empirical biases: over the open sea, the monthly bias between the two estimated total water vapor contents has been subtracted from the 3I 1013–850-hPa-layer water vapor. Doing that, the adjusted 3I total content monthly mean is equal to the SSM/I mean, when available. The same experiment also has been conducted with daily products of SSM/I instead of monthly means; the results are very similar to those presented here (results not shown). This result encourages us to use the SSM/I monthly means, which are more easily tractable, in the future.

The effect of this approach on OLR computed by 3IFlux is illustrated in Fig. 7. The comparison with ERBE data over maritime areas still shows the trend versus the total water vapor content. The agreement between the two determinations is significantly better for the lowest water vapor contents (99 situations), however. The 13 W m$^{-2}$ bias is coherent with the trend, and the standard deviation has been reduced by a factor of 2. No significant change is observed for higher water vapor contents. This study shows that the origin of the 3IFlux deficiency for total water vapor contents smaller than 0.3 cm lies in the high uncertainty in these contents as deduced from TOVS.

## 7. Summary and discussion

At a time when a new generation of satellite instruments is going to be launched, this paper focuses on two methodologies that have been developed at LMD for the estimation of vertical LW radiative fluxes and cooling rates from the TOVS observations. Both of them rely on statistical methods. With N-TbFlux, the whole relationship between the observations and the computed radiative quantities has been parameterized under the form of an MLP. The parameters were determined statistically on the TIGR-3 databank. With 3IFlux, the geophysical variables retrieved by the 3I physico-statistical method are used together with a classical forward radiative transfer code.

The current study has been restricted to the estimation of the clear-sky contribution to the fluxes and cooling rates, a subject about which critical questions currently are being studied. As an example, 3IFlux is used by Chéruy and Chevallier (2000) for the study of the variations of clear-sky infrared cooling as a function of the thermodynamic vertical structure.

In the validation performed, the accuracy of N-TbFlux and 3IFlux overall is comparable to the spread

of the results from the current radiative transfer codes used in GCMs, for OLR and vertical cooling rates. In the case of 3IFlux, the uncertainty of the radiative transfer model has not been studied here and adds to the uncertainty estimated in the current study. Comparisons at TOA with the ERBE instantaneous OLR determinations showed similar uncertainties but smaller biases than in the ERBE process, except for total water vapor contents lower than 0.3 cm. Because of the HIRS poor resolution in the lower atmosphere, higher uncertainty is found for LSNF, up to 10 W $m^{-2}$ standard deviation with N-TbFlux. The 3IFlux and N-TbFlux are both parameterized methods and do not add significant computational burden to the current retrieval process of the TOVS Tbs: one month's worth of data is processed by N-TbFlux in 300 s (central processing unit time) and by 3IFlux in 2200 s (central processing unit time), on a Cray C98 computer.

In the various validations presented here, N-TbFlux performs better than 3I-Flux, with smaller biases in comparison with other data. This difference may be due to the capacity of the neural network–based method to adapt optimally to any vertical pressure grid for the retrieved fluxes, whereas 3I-Flux interpolates between three different grids: the one of the 3I-retrieved temperature, the one of the 3I-retrieved water vapor contents, and the one of the flux computation. Nevertheless, the 3IFlux methodology may be used more easily for climate studies, for which the significance of the signals in the time series has to be asked. Indeed, because of the current lack of high-quality global data of radiative fluxes and cooling rates, the accuracy monitoring of N-TbFlux may be delicate. In comparison, 3IFlux allows for easier quality checks, through the various operational measurements of water vapor, temperature, and surface temperature. As a consequence, as illustrated with the experiment with SSM/I data, 3IFlux allows for bias correction of the final product, whereas the N-TbFlux biases are controlled by the $\delta$s only. In the near future, with the development of flux measurements, with the improvement in the TOVS instrument and in the Advanced TOVS version, and with new infrared sounders such as the Infrared Atmospheric Sounder Interferometer and Advanced Infrared Radiometric Sounder, these two methodologies should produce more accurate results.

*Acknowledgments.* The authors thank A. Chédin who involved the ARA group in the NOAA/NASA Pathfinder program, making such a study possible. The satellite data were provided to us within the framework of this latter program. They are grateful also to J.-J. Morcrette who made the ECMWF radiative code available to them, to R. R. Ferraro for providing the daily SSM/I retrievals, and to C. Paris and E. Brown from NOAA/NESDIS for providing the DSD5 data. The most time-consuming computations have been performed on the Institut du Développement et des Ressources en Informatique Scientifique computers of the Centre National de la Recherche Scientifique.

## REFERENCES

Achard, V., 1991: Trois problèmes clés de l'analyse 3D de la structure thermodynamique de l'atmosphère par satellite: Mesure du contenu en ozone; classification des masses d'air; modélisation hyper rapide du transfert radiatif (Three key problems of the atmosphere thermodynamical structure 3D analysis from satellite observations: Measurement of the ozone content; air-mass classification; very fast modeling of the radiative transfer). Ph.D. thesis, Université Paris VI, 168 pp. [Available from LMD, Ecole Polytechnique, 91128 Palaiseau Cedex, France.]

Alishouse, J. C., S. Snyder, J. Vongsathorn, and R. R. Ferraro, 1990: Determination of oceanic total precipitable water from the SSM/I. *IEEE Trans. Geosci. Remote Sens.,* **28,** 811–816.

Allan, R. P., K. P. Shine, A. Slingo, and A. Pamment, 1999: The dependence of clear-sky outgoing long-wave radiation on surface temperature and relative humidity. *Quart. J. Roy. Meteor. Soc.,* **125,** 2103–2126.

Andersson, E., A. Hollingsworth, G. A. Kelly, P. Lönnberg, J. Pailleux, and Z. Zhang, 1991: Global observing system experiments on operational statistical retrievals of satellite sounding data. *Mon. Wea. Rev.,* **119,** 1851–1864.

Baer, F., N. Arsky, and R. G. Elligson, 1996: Intercomparison of heating rates generated by global climate model longwave radiation codes. *J. Geophys. Res.,* **101,** 26 589–26 603.

Barkstrom, B. R., 1984: The Earth Radiation Budget Experiment (ERBE). *Bull. Amer. Meteor. Soc.,* **65,** 1170–1185.

Chaboureau, J.-P., 1997: Climatologie de la vapeur d'eau atmosphérique à l'échelle globale à l'aide de sondeurs satellitaires (Climatology of the atmospheric water vapor on global scale from satellite sounders). Ph.D. thesis, École Polytechnique, 192 pp. [Available from LMD, Ecole Polytechnique, 91128 Palaiseau Cedex, France.]

——, A. Chédin, and N. A. Scott, 1998: Remote sensing of the vertical distribution of atmospheric water vapor from the TOVS observations. Method and validation. *J. Geophys. Res.,* **103,** 8743–8752.

Chédin, A., N. A. Scott, C. Wahiche, and P. Moulinier, 1985: The Improved Initialization Inversion method: A high resolution physical method for temperature retrievals from satellites of the TIROS-N series. *J. Climate Appl. Meteor.,* **24,** 128–143.

Chéruy, F., and F. Chevallier, 2000: Regional and seasonal variations of the clear-sky atmospheric longwave cooling over tropical oceans. *J. Climate,* **13,** 2863–2875.

——, N. A. Scott, C. Chedin, J.-P. Chaboureau, and C. Stubenrauch, 1994: Coupling the thermodynamic vertical structure of the earth-atmosphere system derived from spaceborne observations with a radiative transfer model for the study of the radiative budget variability. Preprints, *Seventh Conf. on Satellite Meteorology and Oceanography,* Monterey, CA, Amer. Meteor. Soc., 226–228.

——, ——, R. Armante, B. Tournier, and A. Chédin, 1995: Contribution to the development of radiative transfer models for high spectral resolution observations in the infrared. *J. Quant. Spectrosc. Radiat. Transfer,* **53,** 597–612.

——, F. Chevallier, J.-J. Morcrette, N. A. Scott, and A. Chédin, 1996a: A fast method using neural networks for computing the vertical distribution of the thermal component of the Earth radiative budget (in French). *C. R. Acad. Sci., Ser. II,* **322,** 665–672.

——, ——, N. A. Scott, and A. Chédin, 1996b: Use of the vertical sounding in the infrared for the retrieval and the analysis of the longwave radiative budget. *IRS '96: Current Problems in Atmospheric Radiation,* W. L. Smith and K. Stamnes, Eds., A. Deepak, 745–748.

Chevallier, F., 1998: La modélisation du transfert radiatif à des fins climatiques: Une nouvelle approche fondée sur les réseaux de

neurones artificiels (The modeling of radiative transfer for climatic purposes: A new approach based on artificial neural networks). Ph.D. thesis, Université Paris VII, 230 pp. [Available from LMD, Ecole Polytechnique, 91128 Palaiseau Cedex, France.]

——, F. Chéruy, N. A. Scott, and A. Chédin, 1998: A neural network approach for a fast and accurate computation of longwave radiative budget. *J. Appl. Meteor.,* **37,** 1385–1397.

Collins, W. D., and A. K. Inamdar, 1995: Validation of clear-sky fluxes for tropical oceans from the Earth Radiation Budget Experiment. *J. Climate,* **8,** 569–578.

Darnell, W. L., S. K. Gupta, and W. F. Staylor, 1986: Downward longwave surface radiation from sun-synchronous satellite data: Validation of methodology. *J. Climate Appl. Meteor.,* **25,** 1012–1021.

Ellingson, R. G., and J. Ellis, 1991: The intercomparison of radiation codes used in climate models: Longwave results. *J. Geophys. Res.,* **96,** 8929–8953.

——, D. Yanuk, H. T. Lee, and A. Gruber, 1989: A technique for estimating outgoing longwave radiation from HIRS radiance observations. *J. Atmos. Oceanic Technol.,* **6,** 706–711.

——, ——, A. Gruber, and A. J. Miller, 1994: Development and application of remote sensing of longwave cooling from the NOAA polar orbiting satellites. *Photogramm. Eng. Remote Sens.,* **60,** 307–316.

Escobar-Munoz, J., A. Chédin, F. Chéruy, and N. A. Scott, 1993: Réseaux de neurones multicouches pour la restitution de variables thermodynamiques atmosphériques à l'aide de sondeurs verticaux sa tellitaires (Multilayer neural networks for the retrieval of atmospheric thermodynamical variables from satellite vertical sounders). *C. R. Acad. Sci., Ser. II,* **317,** 911–918.

Gruber, A., and J. S. Winston, 1978: Earth–atmosphere radiative heating based on NOAA scanning radiometer measurements. *Bull. Amer. Meteor. Soc.,* **59,** 1570–1573.

Gupta, S. K., 1989: A parameterization for longwave surface radiation from sun-synchronous satellite data. *J. Climate,* **2,** 305–320.

——, A. C. Wilber, W. L. Darnell, and J. T. Suttles, 1992: Longwave surface radiation over the globe from satellite data: An error analysis. *Int. J. Remote Sens.,* **14,** 95–114.

Harrison, E. F., P. Minnis, B. R. Barkstrom, V. Ramanathan, R. D. Cess, and G. G. Gibson, 1990: Seasonal variation of cloud radiative forcing derived from the Earth Radiation Budget Experiment. *J. Geophys. Res.,* **95,** 18 687–18 703.

Hartmann, D. L., and D. Doelling, 1991: On the net radiative effectivness of clouds. *J. Geophys. Res.,* **96,** 869–891.

——, M. E. Ockert-Bell, and M. L. Michelsen, 1992: The effect of cloud type on Earth's energy balance: Global analysis. *J. Climate,* **5,** 1281–1304.

Holton, J. R., 1991: *An Introduction to Dynamic Meteorology.* 3d ed. Academic Press, 391 pp.

Luers, J. K., and R. E. Eskridge, 1998: Use of radiosonde temperature data in climate studies. *J. Climate,* **11,** 1002–1019.

McMillin, L., M. Uddstrom, and A. Coletti, 1992: A procedure for correcting radiosonde reports for radiation errors. *J. Atmos. Oceanic Technol.,* **9,** 801–811.

McPeters, R. D., D. F. Heath, and P. K. Bhartia, 1984: Average ozone profiles for 1979 from the *NIMBUS-7* SBUV instrument. *J. Geophys. Res.,* **89,** 5199–5214.

Mehta, A., and J. Susskind, 1999: Outgoing longwave radiation from the TOVS Pathfinder A dataset. *J. Geophys. Res.,* **104,** 12 193–12 212.

Morcrette, J.-J., 1991: Radiation and cloud radiative properties in the European Centre for Medium Range Weather Forecasts forcasting system. *J. Geophys. Res.,* **96,** 9121–9132.

Moulinier, P., 1983: Analyse statistique d'un vaste échantillonnage de situations atmosphériques sur l'ensemble du globe (Statistical analysis of a large global sample of atmospheric profiles). LMD Internal Note 123, 30 pp. [Available from LMD, Ecole Polytechnique, 91128 Palaiseau Cedex, France.]

Pierrehumbert, R. T., 1995: Thermostats, radiator fins, and the local runaway greenhouse. *J. Atmos. Sci.,* **52,** 1784–1806.

Poore, K. D., J. Wang, and W. B. Rossow, 1995: Cloud layer thickness from a combination of surface and upper air observations. *J. Climate,* **8,** 550–568.

Raschke, E., T. H. Vonder Haar, W. R. Bandeen, and M. Pasternak, 1973: The annual radiation balance of the earth-atmosphere system during 1969–70 from Nimbus 3 measurements. *J. Atmos. Sci.,* **30,** 341–364.

Rieu, H., J. Escobar-Munoz, N. A. Scott, and A. Chédin, 1996: SSM/T forward modelling using neural networks. *J. Quant. Spectrosc. Radiat. Transfer,* **56,** 821–833.

Rossow, W. B., and Y.-C. Zhang, 1995: Calculation of surface and top-of-atmosphere radiative fluxes from physical quantities based on ISCCP datasets: 2. Validation and first results. *J. Geophys. Res.,* **100,** 1167–1197.

Rumelhart, D. E., G. E. Hinton, and R. J. Williams, 1986: Learning internal representations by error propagation. *Parallel Distributed Processing: Explorations in the Microstructure of Cognition 1,* D. E. Rumelhart and J. L. McClelland, Eds., The MIT Press, 318–362.

Scott, N. A., and A. Chédin, 1981: A fast line-by-line method for atmospheric absorption computations: The Automatized Atmospheric Absorption Atlas. *J. Appl. Meteor.,* **20,** 802–812.

——, and Coauthors, 1999: Characteristics of the TOVS Pathfinder Path-B dataset. *Bull. Amer. Meteor. Soc.,* **80,** 2679–2701.

Sinha, A., and J. E. Harries, 1997: The earth's clear-sky radiation budget and water vapor absorption in the far infrared. *J. Climate,* **10,** 1601–1614.

Slingo, A., and M. J. Webb, 1992: Simulation of clear-sky outgoing longwave radiation over the oceans using operational analyses. *Quart. J. Roy. Meteor. Soc.,* **118,** 1117–1144.

——, J. A. Pamment, and M. J. Webb, 1998: A 15-year simulation of the clear-sky greenhouse effect using the ECMWF reanalyses: Fluxes and comparisons with ERBE. *J. Climate,* **11,** 690–708.

Smith, G. L., R. N. Green, E. Raschke, L. M. Avis, J. T. Suttles, B. A. Wielicki, and R. Davies, 1986: Inversion methods for satellite studies of the Earth radiation budget: Development of algorithms for the ERBE mission. *Rev. Geophys.,* **24,** 407–421.

Smith, W. L., H. M. Woolf, C. M. Hayden, D. Q. Wark, and L. M. McMillin, 1979: The TIROS–N operational vertical sounder. *Bull. Amer. Meteor. Soc.,* **60,** 1177–1187.

Soden, B. J., and F. P. Bretherton, 1996: Interpretation of TOVS water vapor radiances in terms of layer-average relative humidities: Method and climatology for the upper, middle, and lower troposphere. *J. Geophys. Res.,* **101,** 9333–9343.

Stephens, G. L., D. L. Jackson, and J. J. Bates, 1994: A comparison of SSM/I and TOVS column water vapor data over the global oceans. *Meteor. Atmos. Phys.,* **54,** 183–201.

Stubenrauch, C. J., W. B. Rossow, F. Chéruy, A. Chédin, and N. A. Scott, 1999a: Clouds as seen by satellite sounders (3I) and imagers (ISCCP). Part I: Evaluation of cloud parameters. *J. Climate,* **12,** 2189–2213.

——, A. Chédin, R. Armante, and N. A. Scott, 1999b: Clouds as seen by satellite sounders (3I) and imagers (ISCCP). Part II: A new approach for cloud parameter determination in the 3I algorithms. *J. Climate,* **12,** 2214–2223.

——, W. B. Rossow, N. A. Scott, and A. Chédin, 1999c: Clouds as seen by satellite sounders (3I) and imagers (ISCCP). Part III: Spatial heterogeneity and radiative effects. *J. Climate,* **12,** 3419–3442.

Susskind, J., P. Piraino, L. Rokke, L. Iredell, and A. Mehta, 1997: Characteristics of the TOVS Pathfinder Path A dataset. *Bull. Amer. Meteor. Soc.,* **78,** 1449–1472.

Tarpley, J. D., 1979: Estimating incident solar radiation from geostationary data. *J. Appl. Meteor.,* **18,** 1172–1181.

Thépaut, J.-N., and P. Moll, 1990: Variational inversion of simulated TOVS radiances using the adjoint techniques. *Quart. J. Roy. Meteor. Soc.,* **116,** 1425–1448.

Tournier, B., R. Armante, and N. A. Scott, 1995: Stransac-93, 4A-

+3,650/351-,5/.8(4734,./. !"#"! $%##&)+*

93. Développement et validation des nouvelles versions des codes de transfert radiatif pour application au projet IASI (Stransac-93, 4A-93. Development and validation of the new versions of the radiative transfer codes for application to the IASI project). LMD Internal Note 201, 43 pp. [Available from LMD, Ecole Polytechnique, 91128 Palaiseau Cedex, France.]

Uddstrom, M. J., and L. M. McMillin, 1993: A collocation archive of radiosonde and satellite data: 1979 to 1993. Users guide. NOAA Tech. Memo. NESDIS, 22 pp. [Available from NOAA/NESDIS, Washington, DC 20233.]

Wahiche, C., 1984: Contribution au problème de la détermination de paramètres météorologiques et climatologiques à partir des données fournies par les satellites de la série TIROS-N, impact de la couverture nuageuse (Contribution to the problem of the retrieval of meteorological and climatological parameters from satellite data from the TIROS-N series: Impact of the cloud cover). Ph. D. thesis. Université Paris VII, 168 pp. [Available from LMD, École Polytechnique, 91128 Palaiseau Cedex, France.]

Wielicki, B. A., R. D. Cess, M. D. King, D. A. Randall, and E. F. Harrison, 1995: Mission to Planet Earth: Role of clouds and radiation in climate. *Bull. Amer. Meteor. Soc.*, **76,** 2125–2153.

Wittmeyer, I. L., and T. H. Vonder Haar, 1994: Analysis of the global ISCCP TOVS water vapor climatology. *J. Climate*, **7,** 325–333.

Wu, X., J. J. Bates, and S. J. S. Khalsa, 1993: A climatology of the water vapor band brightness temperatures from NOAA operational satellites. *J. Climate*, **6,** 1282–1300.

Zhang, Y.-C., W. B. Rossow, and A. A. Lacis, 1995: Calculation of surface and top-of-atmosphere radiative fluxes from physical quantities based on ISCCP datasets: 1. Method and sensitivity to input data uncertainties. *J. Geophys. Res.*, **100,** 1149–1165.

Zhong, W., and J. D. Haigh, 1995: Improved broadband emissivity parameterization for water vapor cooling rate calculations. *J. Atmos. Sci.*, **52,** 124–138.

+3,650/351-,5/.8(4734,./. !"#"! $%##&)+*